A Si/Glass Bulk-Micromachined Cryogenic Heat Exchanger for High Heat Loads: Fabrication, Test, and Application Results

Weibin Zhu, Michael J. White, Gregory F. Nellis, Sanford A. Klein, and Yogesh B. Gianchandani

***Abstract*—This paper reports on a micromachined Si/glass stack recuperative heat exchanger with *in situ* temperature sensors. Numerous high-conductivity silicon plates with integrated platinum resistance temperature detectors (Pt RTDs) are stacked, alternating with low-conductivity Pyrex spacers. The device has a $1 \times 1\text{-cm}^2$ footprint and a length of up to 3.5 cm. It is intended for use in Joule–Thomson (J–T) coolers and can sustain pressure exceeding 1 MPa. Tests at cold-end inlet temperatures of 237 K–252 K show that the heat exchanger effectiveness is 0.9 with 0.039-g/s helium mass flow rate. The integrated Pt RTDs present a linear response of 0.26%–0.30%/K over an operational range of 205 K–296 K but remain usable at lower temperatures. In self-cooling tests with ethane as the working fluid, a J–T system with the heat exchanger drops 76.1 K below the inlet temperature, achieving 218.7 K for a pressure of 835.8 kPa. The system reaches 200 K in transient state; further cooling is limited by impurities that freeze within the flow stream. In J–T self-cooling tests with an external heat load, the system reaches 239 K while providing 1 W of cooling. In all cases, there is an additional parasitic heat load estimated at 300–500 mW. [2009-0093]**

***Index Terms*—Cryosurgery, *in situ* temperature sensing, Joule–Thomson (J–T) cooler, micromachined heat exchanger.**

I. Introduction

THE JOULE–THOMSON (J–T) cooling cycle has applications ranging from cryosurgery [1]–[5] to cooling of infrared detectors in space applications [6]–[8]. Fig. 1 shows the schematic diagram of the J–T cycle and its temperature–entropy (T–s) diagram with ethane as the working fluid. In this cycle, a cold high-pressure fluid leaving a recuperative heat exchanger expands through a valve or an orifice, resulting in a temperature drop if the state of the fluid lies below the J–T inversion curve. The J–T cooling cycle is particularly suitable for applications that require a rapid change in temperature but demand a moderate cooling capacity, possibly with restrictions on size, weight, and structure. With the absence of cold moving parts and the consequent potential for high reliability, J–T coolers are suitable for miniaturization and can be implemented with simple structures that are compatible with silicon/glass microfabrication. Micromachined cryocoolers [9]–[12] have been developed to cool down small integrated circuits in order to improve performance and speed. However, the cooling power of the J–T cycle is proportional to the mass flow rate of the working fluid, and the mass flow rate is smaller than 10 mg/s in these microcoolers; therefore, the cooling power is generally limited to the milliwatt range for the microcoolers that have been demonstrated, even when the input gas pressure is high (2–13.6 MPa). We are interested in a J–T microcooler that can provide relatively high cooling power (100–1000 mW) with modest input gas pressure (1–2 MPa) for cryosurgical or space applications that require a moderate cold-end temperature in the range of 200 K–250 K. In particular, we are interested in facilitating a J–T cooler in this performance range by developing a silicon micromachined heat exchanger that will not only deliver

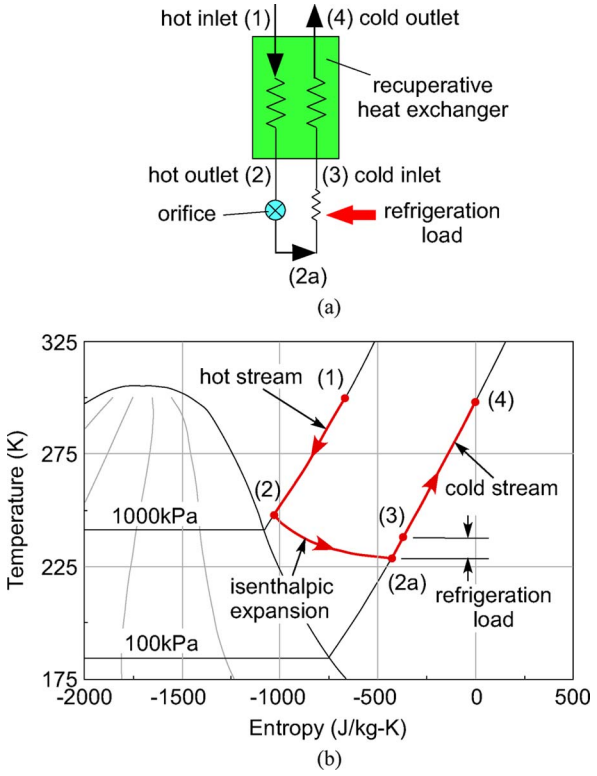

Fig. 1. J–T cycle. (a) Schematic diagram of the J–T cycle. (b) T–s diagram of the J–T cycle with ethane as the working fluid.

Manuscript received April 15, 2009; revised September 4, 2009. First published December 4, 2009; current version published February 3, 2010. This work was supported in part by the U.S. National Institutes of Health under Grant NIH/NINBS R33 EB003349-05. Subject Editor L. Lin.

W. Zhu and Y. B. Gianchandani are with the Department of Mechanical Engineering, University of Michigan, Ann Arbor, MI 48109 USA (e-mail: zhuwb@umich.edu; yogesh@umich.edu).

M. J. White, G. F. Nellis, and S. A. Klein are with the Department of Mechanical Engineering, University of Wisconsin, Madison, WI 53706 USA (e-mail: mjwhite@fnal.gov; gfnellis@engr.wisc.edu; klein@engr.wisc.edu).

Color versions of one or more of the figures in this paper are available online at http://ieeexplore.ieee.org.

Digital Object Identifier 10.1109/JMEMS.2009.2034322

1057-7157/$26.00 © 2009 IEEE

the necessary performance but also include embedded sensors for diagnosis and control.

Counterflow recuperative heat exchangers are commonly used in miniaturized J–T coolers. Ideally, the outlet temperature of the hot stream is very close to the inlet temperature of the cold stream. The hot stream is thus precooled to a very low temperature before it expands through an orifice or valve to produce the J–T cooling effect. In order to achieve high thermal effectiveness [13], [14], these heat exchangers must maintain good stream-to-stream heat conductance between the hot and cold streams while restricting streamwise heat conduction. Microstructures inside the heat exchanger can significantly increase the heat transfer surface area and consequently enhance efficiency. However, low streamwise heat conduction is also necessary for maintaining a large temperature gradient along the heat exchanger and, thus, a low temperature at the cold end. This is particularly challenging in miniature coolers. Prior efforts at miniaturizing heat exchangers have used micromachined glass channels [9], [11], a concentric arrangement of commercial glass tubes [10], optical glass fibers [12], flexible polyimide heat exchangers [15], and planar Si/glass micromachined channels [16]. This paper describes the fabrication method and experimental results for a micromachined perforated-plate stacked Si/glass heat exchanger,[1] designed for superior effectiveness, mass flow rate, and robustness.

Precise temperature measurements within the heat exchanger are necessary in order to diagnose and control its operation as well as validate detailed models of the heat exchanger performance that can be used for design and optimization. Spatially resolved temperature measurements are difficult to obtain in conventional J–T coolers, particularly as their size is reduced. These heat exchangers are made of stainless steel and oxygen-free high-conductivity (OFHC) copper and cannot easily accommodate discrete temperature sensors and the associated lead transfer while maintaining appropriate flow conditions and a high-performance seal. In a micromachined heat exchanger, temperature sensors can monolithically be integrated into the structure during the microfabrication process. The *in situ* temperature-sensing technique allows monitoring of the temperature distribution inside the heat exchanger and, therefore, validation of the heat exchanger model. It also facilitates real-time control of the cooling process.

II. Design

As noted, the first of the two major requirements for an efficient micro heat exchanger is good stream-to-stream heat conductance between the hot and cold streams. The microstructure within the heat exchanger should have a high surface-area-to-volume ratio for effective heat transfer between the structure and the fluid streams. The second requirement is small streamwise conduction inside the heat exchanger. Heat conduction in the fluid direction reduces the temperature gradient between the cold and hot ends and elevates the temperature of the fluid prior to its expansion at the orifice, thereby diminishing the J–T performance.

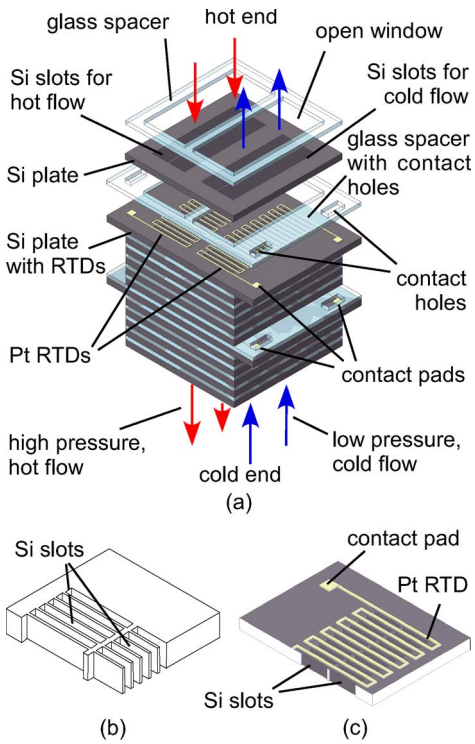

Fig. 2. Perforated-plate heat exchanger design. Platinum resistance temperature detectors (Pt RTDs) are integrated on selected dies. The high-pressure fluid obtained from the external compressor passes through a counterflow recuperative heat exchanger, where it is precooled by the low-pressure fluid returning from the refrigeration load. The cold high-pressure fluid leaving the heat exchanger expands through a valve. The cold low-pressure fluid is directed through the load heat exchanger where it is warmed by the refrigeration load and is then fed back into the heat exchanger. (a) Heat exchanger stack. (b) Si plate sectional view. (c) Si plate with RTD sectional view.

It is helpful to select materials that have appropriate thermal properties to meet these requirements and also are compatible to the microfabrication process. Fortunately, the thermal properties of silicon and Pyrex are reasonable substitutes for those of OFHC copper and stainless steel, respectively, and motivate the use of these materials for a micromachined heat exchanger.

In our design, the perforated-plate stacked Si/glass heat exchanger (Fig. 2) uses numerous high-conductivity silicon plates, alternating with low-conductivity Pyrex glass spacers. Narrow slots are etched into the Si plate in order to provide two sets of passages, i.e., one for the hot stream and the other for the cold stream. The large ratio of perimeter to area that characterizes each of these two sets of slots permits efficient heat transfer between each stream and the Si plate. The streamwise heat conduction is reduced by the glass spacers that have perforations, allowing the hot and cold streams to pass unobstructed from one plate to the next.

A model for the perforated-plate micro heat exchanger used in the J–T cycle was created [20] and implemented in the Engineering Equation Solver software [21]. A detailed numerical model of each plate is based on the technique discussed in [22]. The numerical model is expanded in order to allow a specified heat transfer rate into either end. The individual plate models are integrated by energy balances. The properties of the fluid

[1]Portions of this work were presented in conference abstract form in [17]–[19].

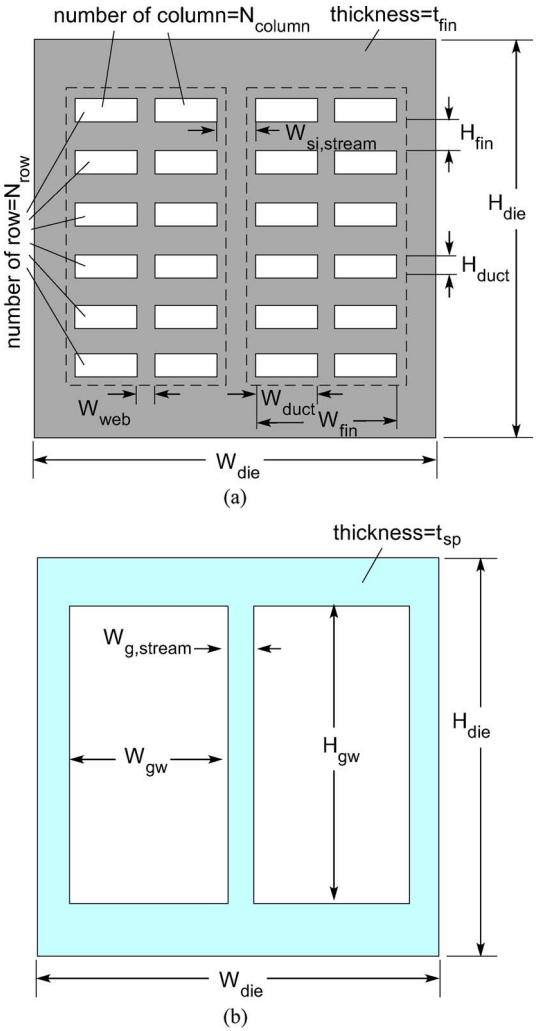

Fig. 3. Simplified patterns of the (a) Si perforated plate and (b) glass spacer.

and material within each plate are assumed constant, but the properties are calculated based on the average temperature and pressure within the plate. The model is capable of predicting the overall performance of the heat exchanger, as well as the spatially resolved temperature distribution in the fluid and heat exchanger material. It explicitly accounts for axial conduction, radiant heat loads, and internal fluid leakage (although this effect is not present in the heat exchangers considered in this paper). The heat transfer coefficients and pressure drop are calculated using correlations for developing internal flow. Additional details regarding the model can be found in [23].

The model was used to determine the geometric details of the design, including the number and size of the slots, the distance between slots, the number of plates, etc. [20]. The estimated dimensions of the pattern of the Si plate and the glass spacer after the fabrication process are shown in Fig. 3 and summarized in Table I. (Dies integrated with Pt RTDs have slightly different dimensions and can selectively be bonded to the heat exchanger for precise and real-time measurement of the temperature distribution inside the heat exchanger.) There are many different slot-pattern configurations that can be envisioned for the silicon plates. For example, the two fluid regions could be concentric, with the colder region at the center and the warmer region at the perimeter. The slot pattern shown in Fig. 3 was chosen for several reasons: 1) Anisotropic wet etching process is used to fabricate the silicon slot pattern. The orientation of the slot pattern is, therefore, constrained by the crystal orientation of silicon. 2) Leakage between the two flow regions is a potential weakness of the perforated plate heat exchanger. The rectangular configuration shown in Fig. 3 minimizes the bonding interface between the two regions, thus reduces the possibility of internal leakage between the two streams. 3) The silicon and glass plates are generally diced into rectangular or square dies. Compared to the circular configuration, this design can better utilize the available space within a die.

TABLE I
ESTIMATED DIMENSIONS OF THE Si PERFORATED PLATE AND GLASS SPACER AFTER THE FABRICATION PROCESS

Si plate		Glass spacer	
Variables	Dimension	Variables	Dimension
W_{die}	9770 μm	W_{die}	9770 μm
H_{die}	9770 μm	H_{die}	9770 μm
$W_{si,stream}$	1500 μm	$W_{g,stream}$	700 μm
W_{duct}	1400 μm	W_{gw}	3700 μm
H_{duct}	50 μm	H_{gw}	8150 μm
W_{web}	10 μm	t_{sp}	300 μm
W_{fin}	2900 μm		
H_{fin}	50 μm		
t_{fin}	500 μm		
N_{column}	2		
N_{row}	74		

Effectiveness, the figure of merit that is most commonly used to evaluate the performance of heat exchangers, is defined as the ratio of the rate of heat transfer within the heat exchanger to the maximum possible rate of heat transfer. The effectiveness values are calculated based on the hot and cold heat transfer rates, respectively,

$$\varepsilon_h = \frac{\dot{q}_{h,\text{net}}}{\dot{q}_{\max}} = \frac{\dot{m}_h(i_{h,\text{in}} - i_{h,\text{out}})}{\dot{q}_{\max}} \tag{1}$$

$$\varepsilon_c = \frac{\dot{q}_{c,\text{net}}}{\dot{q}_{\max}} = \frac{\dot{m}_c(i_{c,\text{out}} - i_{c,\text{in}})}{\dot{q}_{\max}} \tag{2}$$

where $\dot{m}_h$ and $\dot{m}_c$ are the hot- and cold-side mass flow rates, respectively; $(i_{h,\text{in}} - i_{h,\text{out}})$ and $(i_{c,\text{out}} - i_{c,\text{in}})$ are the enthalpy changes of the hot and cold fluids, respectively; and $\dot{q}_{\max}$ is the maximum possible rate of heat transfer that occurs if the hot fluid is cooled to the cold inlet temperature or the cold fluid is warmed to the hot inlet temperature (whichever result provides the smaller value). Equations (1) and (2) are used to compute the effectiveness with the numerical model. In the limit where the specific heat of the working fluid is constant across the length of the heat exchanger, the hot- and cold-side effectiveness can be calculated according to

$$\varepsilon_h = \frac{T_{h,\text{in}} - T_{h,\text{out}}}{T_{h,\text{in}} - T_{c,\text{in}}} \tag{3}$$

$$\varepsilon_c = \frac{T_{c,\text{out}} - T_{c,\text{in}}}{T_{h,\text{in}} - T_{c,\text{in}}} \tag{4}$$

where $T_{h,\text{in}}$ and $T_{h,\text{out}}$ are the hot-fluid inlet and outlet temperatures, respectively, and $T_{c,\text{in}}$ and $T_{c,\text{out}}$ are the cold-fluid inlet and outlet temperatures, respectively. The hot- and

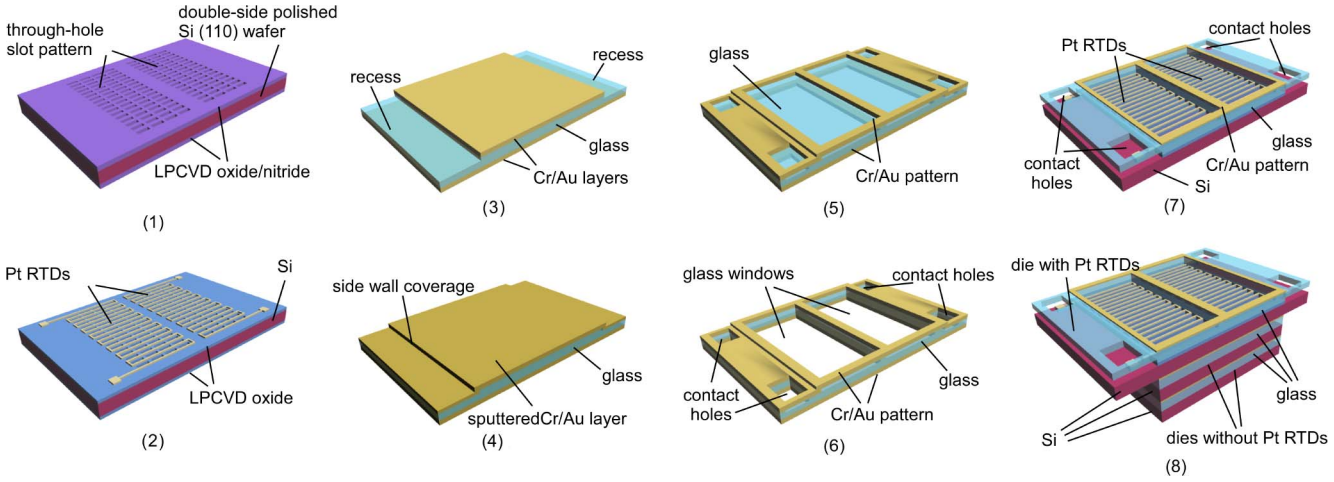

Fig. 4. Fabrication process of the perforated-plate Si/glass heat exchanger with Pt RTDs. (1) Oxide/nitride mask are deposited and patterned by RIE. Si wafer is etched through in KOH, oxide/nitride mask is then removed. (2) LPCVD oxide is deposited, then Pt RTDs are patterned on the oxide layer. (3) Cr/Au layers are deposited on both sides. Cr/Au layer on the top is patterned, a glass recess is etched down 20 microns. The Cr/Au layer on the top side is then removed. (4) New Cr/Au layer is sputtered on the top side for good side wall coverage. (5) Cr/Au layers on both sides are then patterned. (6) Glass wafer is etched through from both sides in HF : HNO_3, Cr/Au layers are then removed. (7) Glass wafer is flipped and anodically bonded to the Si wafer. Cr/Au layer is patterned on the top of glass for Si-Au eutectic bonding (not needed for epoxy). (8) Wafer is diced. Dies are stacked and bonded together.

cold-side effectiveness values will not be generally the same due to parasitic heat transfer that is preferentially picked up by one of the streams.

The average temperatures on both sides of each die in the heat exchanger can be calculated from the model based on the inlet and outlet conditions. By comparing to the experimental results measured from the Pt RTDs, the numerical model can be verified directly using spatially resolved information about the temperature distribution.

The simulation results of the effectiveness and temperature distribution within different heat exchangers were validated against the experimental results in [20] and [23], showing good agreement. The comparisons were performed for both helium and ethane as cooling gases; the simulations matched the helium tests most closely and were within a few percent of the experimental measurements in some cases.

III. Fabrication

There are two general challenges in the fabrication of the perforated-plate heat exchanger. First, the uniformity of the structure must be maintained across relatively large regions. The footprint of the device is as large as 1 cm, while the desired precision of fabricating the silicon slot patterns is as small as ± 1 μm. Second, there are numerous bonding interfaces between the silicon plates and glass spacers that must sustain high pressure difference without failure or leakage. A four-mask six-step fabrication process [17], [18] is described for this heat exchanger (Fig. 4). A double-side KOH wet-etching process on (110) Si wafers provides slot patterns with high uniformity and high yield and accommodates a variety of bonding techniques, including Si-glass anodic bonding, epoxy, and Si–Au eutectic bonding to form strong seals in the following different process steps.

1) The Si slot patterns are etched through by a double-side KOH process on (110) Si wafers, using the following steps. A 500-μm-thick double-side polished (110) Si wafer is covered first with an 800-nm LPCVD oxide layer, followed by a 200-nm nitride layer. The patterns on both sides are mirror images such that a single laterally symmetrical lithographic mask can be designed for these two patterning steps; an accurate alignment is critical. The dielectrics are then dry etched, exposing the Si surface in slot patterns. When the wafers are inserted in 50% KOH solution, the exposed regions are simultaneously etched through from both sides of the wafer, and vertical sidewalls are formed on long edges of the slots. In general, a single-side KOH etch of (110) Si results in six facets, out of which four are perpendicular to the surface [24], [25]. The double-side KOH process in this fabrication step can reduce the etch time to half and partially or completely remove the nonperpendicular facets, depending on the total etching time. This is because, when the wafer is etched through, the two symmetrical nonperpendicular facets, including one on the top and the other on the bottom side, will encounter and be attacked by the KOH solution. The total etch time to etch through the 500-μm-thick Si wafer is approximately 5–6 h. Our experiments indicate that this wet-etching process is more cost effective and can achieve much better uniformity across the wafer than plasma dry etching. The oxide/nitride dielectrics are stripped after the KOH process. The inset in Fig. 5(a) shows an SEM of the fabricated slot structure.
2) Oxide layers of 100 nm thickness are deposited on both sides of the silicon wafer for electrical insulation. A 5-nm/100-nm Ti/Pt thin film is deposited on one side and patterned (in a lift-off process) to form Pt RTDs on selected dies.
3) The glass spacers are fabricated using 300-μm-thick Pyrex wafers. First, Cr/Au layers are deposited as etch masks on both sides of the Pyrex wafer. The Cr/Au layer

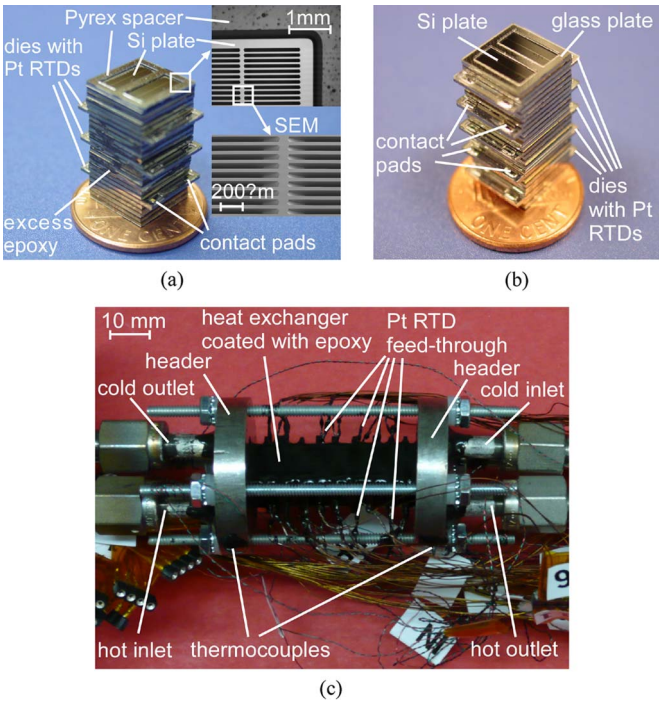

Fig. 5. Die size of the perforated-plate micro heat exchanger is 1×1 cm^2. The thickness of the Si plate in each die is 500 μm. The thickness of the Pyrex spacer is 300 μm. Two rows of opening slots are on each side of the Si plate. The slot is 50 μm wide and 1400 μm long; there is 50-μm gap between each slot. The dies with Pt RTDs are equally distributed across the entire length of the micro heat exchanger. (a) Heat exchanger bonded by STYCAST 2850FT epoxy. The total length is about 2 cm (25 dies). (b) Heat exchanger fabricated by Si–Au eutectic bonding. The total length is about 2 cm (25 dies). (c) Heat exchanger mounted to a pair of stainless steel headers. The heat exchanger is about 3.5 cm long (with 43 dies) and coated with epoxy for thermal and electrical insulation. Thermocouples are inserted into the header to measure the inlet and outlet temperatures.

on the front side is patterned, and 20-μm-deep recesses are etched using a $HF:HNO_3$ wet-etching process. The Cr/Au mask on the front side is then removed.

4) A new Cr/Au layer is sputtered on the front side, and good sidewall coverage on these shallow recesses is achieved.
5) The Cr/Au layers on both sides are patterned by a single mask to form the mirror images on the front and back sides of the wafer.
6) The glass wafer is simultaneously wet etched from both sides in $HF:HNO_3$ to form the through-wafer perforations. The total etch time is restricted to about 30 min to prevent the Cr/Au masks from peeling off from the wafer.
7) The patterned Si and glass wafers are then anodically bonded together. The two-wafer stack is then diced into individual dies.
8) The two-wafer dies are finally assembled into bonded stacks containing up to 43 pieces. The number of pieces in these stacks was selected to represent different lengths; this parameter can be changed as needed for any particular application. Two different methods are used for bonding the Si/glass stack: epoxy and Si–Au eutectic. Fig. 5(a) shows a fabricated 1×1 cm^2 heat exchanger with 2 cm bonded by epoxy STYCAST 2850FT (Emerson & Cuming, Inc., Billerica, MA). Dies with Pt RTDs are also interleaved in this stack and are evident from the protrusions provided for lead transfer on each such die. When Si–Au eutectic bonding [26], [27] is used, the entire stack can be bonded in a single thermal step. This requires an extra mask for patterning the gold layer before dicing. A 1×1 cm^2 heat exchanger with 2 cm bonded by this method is shown in Fig. 5(b). Since the yield of the die-level Si–Au eutectic bonding on a stack is relatively low due to the limitation of available process equipment, fabricating a very long heat exchanger stack with this method is still challenging. The heat exchanger stack is mounted to a pair of stainless-steel headers that are connected to the test facility with standard fittings. Fig. 5(c) shows a heat exchanger with 43 dies that is mounted to the headers.

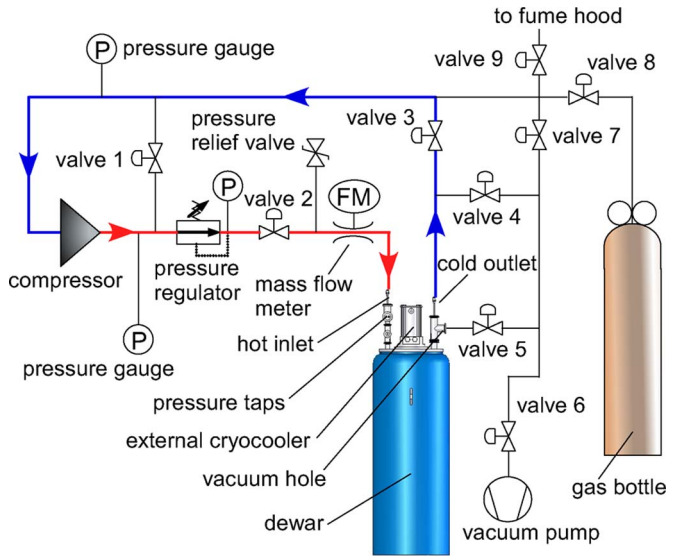

Fig. 6. Flow schematic of the test facility.

IV. Experimental Method and Setup

Two types of test procedures are used to evaluate the fabricated heat exchangers. The first is an experimental measurement of the heat exchanger effectiveness over a range of mass flow rates. In this test, an external cryocooler and a heater are used to control large temperature differences across the heat exchanger while minimizing the pressure drop across it (to 100–250 kPa). The second is a J–T self-cooling test intended to evaluate the cooling performance under varying loads and conditions. In this test, an orifice is used for gas expansion, and the input gas pressure provided by a compressor is as high as 1 MPa.

A test facility was developed to accommodate both test procedures. An essential element of the test facility is a Dewar, which is evacuated to less than 1 mtorr to reduce the parasitic heat load on the heat exchanger. The flows outside and inside the Dewar are shown in Figs. 6 and 7, respectively. An HC-2D compressor manufactured by APD Cryogenics, Inc. and a pressure regulator are used to control the inlet pressure (Fig. 6). High vacuum and multi-layer insulations between the assembly and the Dewar (represented by the dashed line in Fig. 7) are used for thermal insulation. In the effectiveness

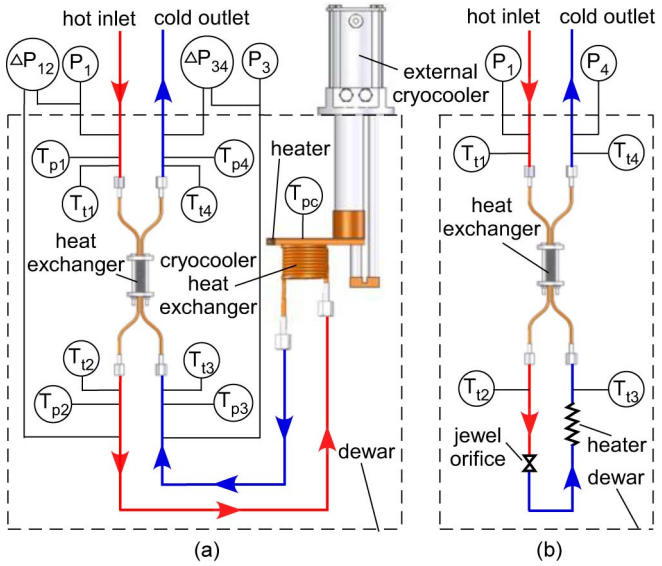

Fig. 7. Flow schematic of the components inside the Dewar. (a) Effectiveness test: Helium is used as the working fluid. $\Delta P_{12} = P_1 - P_2$. $\Delta P_{34} = P_3 - P_4$. (b) Self-cooling test: ethane is used as the working fluid.

test [Fig. 7(a)], the fluid leaving the hot side of the heat exchanger is cooled down to cryogenic temperature by the external cryocooler before it flows back to the cold side of the heat exchanger. Helium is used in this test. In the self-cooling test [Fig. 7(b)], the working fluid flows through a very small opening provided by a jewel orifice in order to generate a pressure drop and, therefore, a J–T effect. The self-cooling test employs the heat exchanger within a J–T cycle. A variable heater is located downstream of the orifice in order to simulate an external heat load. The inlet pressure is adjusted by the pressure regulator and the external compressor. While it is recognized that an optimized mixture of working gases can significantly enhance system performance [28]–[30], pure ethane is used for simplicity in this test procedure. This system has been robust and reliable with more than 240 h of uninterrupted operations without failure and leakage.

In both types of test procedures, temperatures at the hot inlet (of the heat exchanger, $T_{h,\mathrm{in}}$), hot outlet $(T_{h,\mathrm{out}})$, cold inlet $(T_{c,\mathrm{in}})$, and cold outlet $(T_{c,\mathrm{out}})$ are measured. In Fig. 7, these four locations are denoted by subscripts 1, 2, 3, and 4, respectively. For measurements of effectiveness, two sets of temperature measurements are recorded simultaneously: the first, using commercially-available platinum resistance thermometers (PRTs), denoted by T_p; the second, using thermocouples, denoted by T_t. The PRTs are calibrated by the manufacturer and offer uncertainties of ± 0.25 K. The thermocouples are made from the same spool of thermocouple wire. The absolute uncertainties of these thermocouples are ± 1 K. Both the readings from the PRTs and the thermocouple are measured using an Agilent 34970A multiplexer. Due to limited available ports in the multiplexer, the J–T self-cooling test procedure utilizes only the thermocouples to measure temperatures outside the heat exchanger, while the effectiveness test utilizes both the PRTs and the thermocouples. The readings from the Pt RTDs that are integrated with the Si plates are simultaneously measured by the multiplexer in both tests.

Pressure measurements are made at the locations shown in Fig. 7. Digital pressure gauges are used to measure the absolute and differential pressures, and the gauges have $\pm 0.11\%$ full scale uncertainty. The mass flow rate is measured by a Bronkhorst F-132M mass flow meter that is calibrated with nitrogen. The mass-flow-rate reading and its uncertainty are converted to the ones for the corresponding fluid based on formulas recommended by the manufacturer.

V. Experimental Results

Although several heat exchangers with different lengths have been fabricated and tested, all the experimental results discussed in this paper are for heat exchangers fabricated from 43 stacked dies, i.e., with 43 pieces each of Si and glass [Fig. 5(c)]. In the effectiveness tests, the hot-inlet temperature was maintained at around 300 K, whereas the cold-inlet temperature was controlled in the range of 237 K–252 K by adjusting the temperature at the cold stage of the external cryocooler. Because the temperature measurements from the PRTs and thermocouples are almost identical, the effectiveness calculated from these two sets of measurements overlap in Fig. 8(a). The maximum measured effectiveness of the heat exchanger based on the cold stream (ε_c) is 0.9 at 0.039-g/s helium mass flow rate.

The effectiveness based on the hot side (ε_h) and the cold side (ε_c) does not match exactly due to the parasitic heat load on the heat exchanger that causes more heat to be transferred to the cold stream and less heat to be removed from the hot stream. The parasitic heat loads are nearly constant across all data points. At smaller mass flow rates, the parasitic heat loads are a significant fraction of the total heat transferred between the fluid streams, which explains the larger spread [shown in Fig. 8(a)] between the measured effectiveness at smaller mass flow rates. The effectiveness on both sides of the heat exchanger is nearly identical at higher flow rates because the parasitic heat loads are small relative to the heat transferred between the streams at higher flow rates.

Before any test, the integrated Pt RTDs for *in situ* temperature sensing in the heat exchanger were simultaneously calibrated by comparison with the externally installed commercial PRTs over the range of 205 K–296 K. The sensors have a typical sensitivity of 0.26%–0.30%/K and remain linear over the range of 80 K–300 K. Fig. 8(b) shows the typical temperature distribution measured inside the heat exchanger during the effectiveness test. The inlet and outlet temperatures were measured by the commercial PRTs, whereas temperatures inside the heat exchanger were measured by the integrated Pt RTDs.

In J–T self-cooling tests that were performed without an external heat load, three commercially available orifices with different diameters (0.010, 0.015, and 0.020 in; Bird Precision Corporation) were used. The corresponding opening areas of these three orifices are 0.0507, 0.1140, and 0.2027 mm^2, respectively. Fig. 9(a) shows the steady-state temperature drop $(T_{t1} - T_{t3})$ as a function of pressure difference between the hot inlet and cold outlet $(P_1 - P_4)$ for these three orifices. Instead of absolute temperature, the temperature drop from

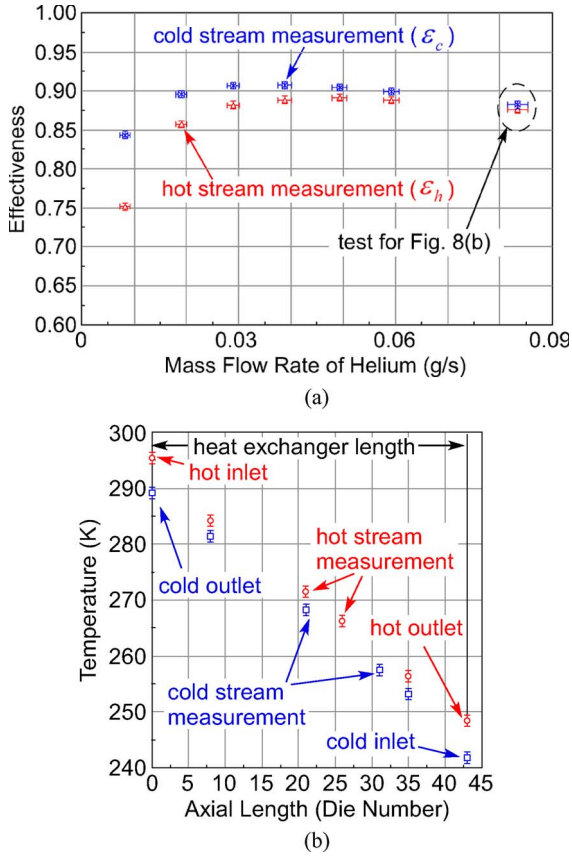

Fig. 8. Effectiveness tests over a range of helium mass flow rates. (a) Effectiveness as a function of helium mass flow rate. Two independent sets of data are measured from thermocouples (T_t) and PRTs (T_p), but they are almost identical. The effectiveness measured by thermocouples is calculated as $\varepsilon_h = (T_{t1} - T_{t2})/(T_{t1} - T_{t3})$ on the hot stream and $\varepsilon_c = (T_{t4} - T_{t3})/(T_{t1} - T_{t3})$ on the cold stream. The effectiveness measured by the PRTs can be calculated in similar equations. The hot-inlet temperature is at room temperature, whereas the cold-inlet temperature is allowed to vary over 237 K–252 K. (b) Measured temperature distributions inside the heat exchanger at the highest measured flow rate [Fig. 8(a)]. The temperatures are measured by the integrated Pt RTDs. The inlet and outlet temperatures are measured by the thermocouples shown in Fig. 7(a).

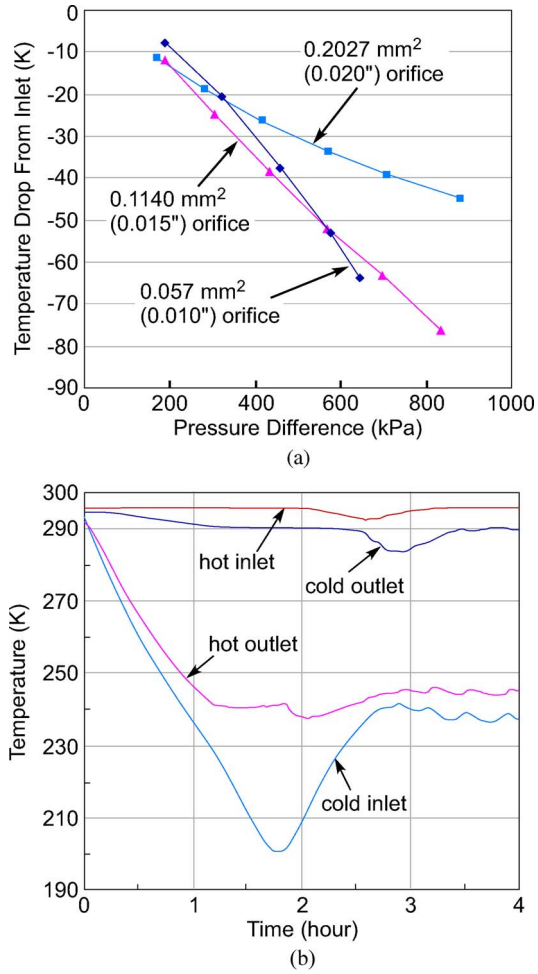

Fig. 9. J–T self-cooling test. (a) Temperature drop at the orifice from the inlet temperature $(T_{t3} - T_{t1})$ as a function of pressure difference between inlet and outlet $(P_1 - P_4)$ in the self-cooling test. (b) Transient temperature profile of the heat exchanger in the J–T self-cooling test with 0.057-mm^2 (0.010 in diameter) orifice.

the hot-inlet temperature is used in this plot to accommodate variations in the inlet temperature. The inlet temperature varied in the range of 294 K–296 K, as it was affected by the room temperature. In these tests, the cold-outlet pressure was kept about 10 kPa higher than atmospheric pressure. The maximum measured temperature drop was 76.1 K from the inlet temperature (corresponding to an actual temperature of 218.7 K) at 0.269-g/s ethane mass flow rate, while the pressure difference was 835.8 kPa (121.5 lbf/in^2 difference) and the hot-inlet pressure (P_1) was at 1 MPa (145 lbf/in^2 absolute). The measured curve [Fig. 9(a)] tends to be steeper as the orifice size is reduced. This is because, in the given pressure range, the higher flow rate associated with a larger orifice tends to diminish the effectiveness of the heat exchanger. Conversely, a smaller orifice reaches the optimal flow rate and effectiveness at a larger pressure difference; it achieves lower temperature but offers lower cooling power. Optimal sizing of the orifice will depend on the temperature and cooling power necessary for the desired application.

Fig. 9(b) shows the transient temperature profile as the J–T system with 0.0507-mm^2 (0.010 in diameter) orifice is cooled down from the room temperature without an external heat load. The hot-inlet gas pressure is about 1 MPa. As the hot-outlet temperature approaches 244 K, freezing of impurities in the fluid stream begins to reduce the fluid mass flow rate. However, the cold-inlet temperature continues to drop to 200 K due to the J–T effect. At this point, the mass flow rate is sufficiently low such that the temperature rises, allowing sufficient thawing to permit the fluid to flow again. Clogging due to impurities is very common in closed-loop microcoolers. A similar clogging phenomenon was reported in [31], and trapped water vapor freezing around the flow restriction was the cause of the clogging in that case. This is not a fundamental limitation of the heat exchanger performance and can be fixed by adding a cold trap to remove the impurities from the fluid stream. However, an extensive J–T test is beyond the scope of this paper.

There are three significant parasitic heat loads in our tests, including radiation from the vacuum-insulated vessel wall, thermal conduction through the header and the Pt RTD feedthroughs, and ohmic dissipation from the integrated Pt RTDs. While the radiation can be minimized to the microwatt

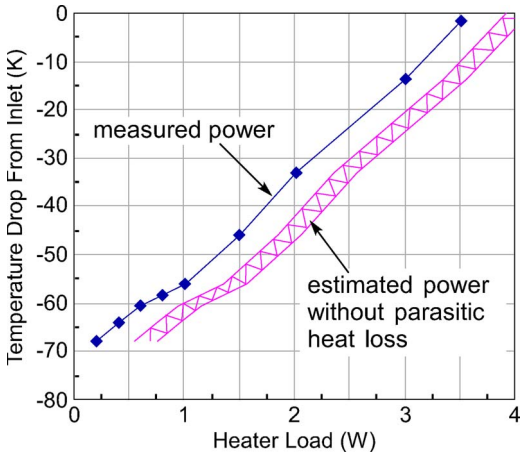

Fig. 10. Temperature drop at the orifice from the inlet temperature (which was 295 K–296 K) as a function of external heat load in the J–T self-cooling test using a 0.1140-mm^2 (0.015 in diameter) orifice.

range using multi-layer insulation as a radiation shield, the thermal conduction and the ohmic dissipation are difficult to eliminate. The total parasitic heat load for the heat exchanger can be estimated based on the enthalpy rise of the fluid measured in the effectiveness test; the enthalpy rise is computed using the temperatures and pressures that are measured at the inlets and outlets of the heat exchanger. According to the measurements performed in the effectiveness test, the estimated parasitic heat load is between 300 and 500 mW.

As noted previously, the ability of the heat exchanger to tolerate higher heat loads can be evaluated by using an external heater together with the J–T system. Fig. 10 shows the temperature drop from the inlet temperature in a J–T self-cooling test with 0.1140-mm^2 (0.015 in diameter) orifice. The measurements show that the system can provide cooling powers of 200 mW at 228 K and 1 W at 239 K in addition to the estimated parasitic heat load of 300–500 mW.

VI. Discussion and Conclusion

This effort has resulted in the successful fabrication of a micromachined perforated-plate stacked Si/glass heat exchanger integrated with Pt RTDs. The fabricated heat exchanger has a footprint of 1×1 cm^2 and a length of up to 3.5 cm. In the effectiveness tests, the heat exchangers have demonstrated a typical effectiveness of 0.9 in a cryogenic temperature range of 237 K–252 K and were robust to high working pressures (up to 1 MPa). Real-time *in situ* temperature measurement within the heat exchanger has been demonstrated by the embedded sensors with sensitivities of 0.26%–0.30%/K across the cryogenic temperature range of 205 K–296 K. In J–T self-cooling tests without an external heat load, a system with this heat exchanger has reached 76 K below room temperature (approximately 218.7 K) at 835.8 kPa (121.5 lbf/in^2 difference) in steady state and about 200 K in transient state, but the lower temperature has been limited by the presence of either contamination or liquid build-up. The system has provided cooling powers of 200 mW at 228 K and 1 W at 239 K in addition to a parasitic heat load of 300–500 mW that was present due to the experimental set-up.

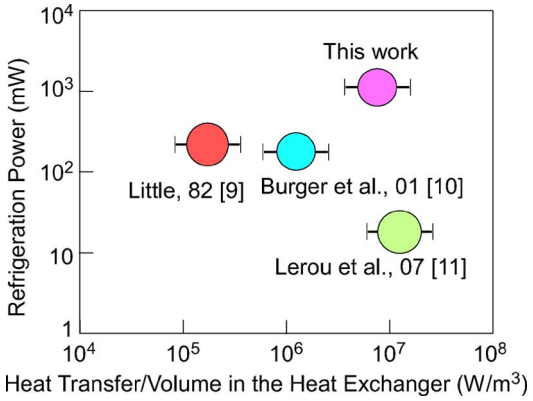

Fig. 11. Comparison of the micromachined heat exchangers used in the microcoolers.

Total heat transfer per unit volume in a heat exchanger is an important characteristic to describe the performance of the heat exchanger. Fig. 11 shows the refrigeration power of several existing micromachined coolers that were reported in the past, as a function of heat transfer per unit volume of the heat exchangers. The total heat transfer within the heat exchangers that were presented in literature has been estimated from mass flow rate, the specific heat of the working fluid at the average temperature on the cold side, and the temperature difference between the inlet and outlet of the cold side of the heat exchanger. Due to the limited information that was published, several assumptions have been made for this calculation: 1) The outlet temperature and pressure on the cold side are 20 °C and 100 kPa, unless otherwise specified; 2) mass flow rate is constant in the system, i.e., there is no external leakage; and 3) parasitic heat load in the heat exchanger is negligible. The volume of the heat exchangers reported in the literature is estimated from the total size of the micromachined coolers. As shown in Fig. 11, when simultaneously evaluating the refrigeration power and the heat transfer per unit volume, the micromachined perforated-plate heat exchanger demonstrates very promising performance and could be suitable for a wide range of cooling applications that require a large cooling power and a compact size.

In conclusion, this perforated-plate heat exchanger has achieved high effectiveness and has consequently provided significant cooling powers with moderate input gas pressures. In the long term, this design is particularly suitable for fully micromachined closed-loop J–T coolers that demand low input gas pressure, limited by micromachined compressors. By integrating an orifice or flow restriction and through the use of an appropriately optimized gas mixture, this perforated-plate heat exchanger should be able to provide substantial cooling capacity, beyond what is reported here. Many potential applications, including cryosurgery and cooling infrared detectors for space applications, will significantly benefit from these findings.

Acknowledgment

The authors would like to thank D. W. Hoch for participating in the design and modeling of the heat exchanger.

REFERENCES

[1] A. A. Gage, "Cryosurgery in the treatment of cancer," *Surg. Gynecol. Obstet.*, vol. 174, no. 1, pp. 73–92, Jan. 1992.

[2] Z. H. Chang, J. J. Finkelstein, and J. G. Baust, "Optimization of cryosurgical instrumentation for use in minimally invasive prostate surgery," *ASME Heat Transfer Div. Publ. HTD*, vol. 267, pp. 45–55, 1993.

[3] J. Dobak, "A review of cryobiology and cryosurgery," *Adv. Cryog. Eng.*, vol. 43, pp. 889–896, 1998.

[4] B. Z. Maytal, "Fast Joule–Thomson cryocycling device for cryosurgical applications," *Adv. Cryog. Eng.*, vol. 43, pp. 911–917, 1998.

[5] E. D. Marquardt, R. Radebaugh, and J. Dobak, "A cryogenic catheter for treating heart arrhythmia," *Adv. Cryog. Eng.*, vol. 43, pp. 903–910, 1998.

[6] B. Collaudin and N. Rando, "Cryogenics in space: A review of the missions and of the technologies," *Cryogenics*, vol. 40, no. 12, pp. 797–819, 2000.

[7] M. Klauda, T. Kässer, B. Mayer, C. Neumann, F. Schnell, B. Aminov, A. Baumfalk, H. Chaloupka, S. Kolesov, H. Piel, N. Klein, S. Schornstein, and M. Bareiss, "Superconductors and cryogenics for future communication systems," *IEEE Trans. Microw. Theory Tech.*, vol. 48, no. 7, pp. 1227–1239, Jul. 2000.

[8] H. J. M. ter Brake and G. F. M. Wiegerinck, "Low-power cryocooler survey," *Cryogenics*, vol. 42, no. 11, pp. 705–718, Nov. 2002.

[9] W. A. Little, "Microminiature refrigeration—Small is better," *Physica*, vol. 109 & 110B, pp. 2001–2009, 1982.

[10] J. F. Burger, H. J. Holland, J. Seppenwoolde, E. Berenschot, H. J. M. ter Brake, J. Gardeniers, M. Elwenspoek, and H. Rogalla, "165 K microcooler operating with a sorption compressor and a micromachined cold stage," in *Cryocoolers*, vol. 11. New York: Plenum, 2001, pp. 551–560.

[11] P. P. P. M. Lerou, H. J. M. ter Brake, J. F. Burger, H. J. Holland, and H. Rogalla, "Characterization of micromachined cryogenic coolers," *J. Micromech. Microeng.*, vol. 17, no. 10, pp. 1956–1960, Oct. 2007.

[12] P. E. Bradley, R. Radebaugh, M. Huber, M.-H. Lin, and Y. C. Lee, "Development of a mixed-refrigerant Joule–Thomson microcryocooler," in *Proc. 15th Int. Cryocoolers Conf.*, Long Beach, CA, 2008, pp. 425–432.

[13] F. P. Incropera and D. P. DeWitt, *Fundamentals of Heat and Mass Transfer*, 4th ed. New York: Wiley, 1996.

[14] R. F. Barron, *Cryogenic Heat Transfer*. New York: Taylor & Francis, 1999.

[15] J. C. Selby, M. L. Philpott, and M. A. Shannon, "Fabrication of mesoscopic, flexible, high pressure, microchannel heat exchangers (MHEx)," *Trans. NAMRI/SME*, vol. 29, pp. 469–476, 2001.

[16] W. Zhu, D. W. Hoch, G. F. Nellis, S. A. Klein, and Y. B. Gianchandani, "A planar glass/Si micromachining process for the heat exchanger in a J–T cryosurgical probe," in *Proc. Solid-State Sens., Actuators, Microsyst. Workshop*, Hilton Head Island, SC, 2006, pp. 51–55.

[17] W. Zhu, M. J. White, D. W. Hoch, G. F. Nellis, S. A. Klein, and Y. B. Gianchandani, "Two approaches to micromachining Si heat exchangers for Joule–Thomson cryosurgical probes," in *Proc. IEEE Conf. Micro Electro Mech. Syst.*, Kobe, Japan, Jan. 2007, pp. 317–320.

[18] W. Zhu, M. J. White, G. F. Nellis, S. A. Klein, and Y. B. Gianchandani, "A perforated plate stacked Si/glass heat exchanger with *in situ* temperature sensing for Joule–Thomson coolers," in *Proc. IEEE Conf. Micro Electro Mech. Syst.*, Tucson, AZ, Jan. 2008, pp. 844–847.

[19] W. Zhu, M. J. White, G. F. Nellis, S. A. Klein, and Y. B. Gianchandani, "A Joule–Thomson cooling system with a Si/glass heat exchanger for 0.1–1 W heat loads," in *Proc. 15th Int. Conf. Solid-State Sens., Actuators, Microsyst. (TRANSDUCERS)*, Denver, CO, Jun. 2009, pp. 2417–2420.

[20] M. J. White, G. F. Nellis, S. A. Klein, W. Zhu, and Y. B. Gianchandani, "An experimentally validated numerical modeling technique for perforated plate heat exchangers," *J. Heat Transfer*, manuscript approved, to be published.

[21] S. A. Klein and F. L. Alvarado, "EES—Engineering Equation Solver," F-Chart Software2002. [Online]. Available: http://www.fchart.com

[22] G. F. Nellis, "A heat exchanger model that includes axial conduction, parasitic heat loads, and property variations," *Cryogenics*, vol. 43, no. 9, pp. 523–538, Sep. 2003.

[23] M. J. White, "Performance of a MEMS heat exchanger for a cryosurgical probe," M.S. thesis, Univ. Wisconsin, Madison, WI, 2008.

[24] M. Madou, *Fundamentals of Microfabrication*. Boca Raton, FL: CRC Press, 1997.

[25] F. S.-S. Chien, C.-L. Wu, Y.-C. Chou, T. T. Chen, S. Gwob, and W.-F. Hsieh, "Nanomachining of (110)-oriented silicon by scanning probe lithography and anisotropic wet etching," *Appl. Phys. Lett.*, vol. 75, no. 16, pp. 2429–2431, Oct. 1999.

[26] R. F. Wolffenbuttel and K. D. Wise, "Low temperature silicon wafer-to-wafer bonding using gold at eutectic temperature," *Sens. Actuators A, Phys.*, vol. 43, no. 1–3, pp. 223–229, May 1994.

[27] J. Mitchell, G. R. Lahiji, and K. Najafi, "Encapsulation of vacuum sensors in a wafer level package using a gold-silicon eutectic," in *Proc. TRANSDUCERS*, Jun. 2005, vol. 1, pp. 928–931.

[28] W. A. Little, "Recent developments in Joule–Thomson cooling: Gases, coolers, and compressors," in *Proc. 5th Int. Cryocooler Conf.*, 1988, pp. 3–11.

[29] M. Q. Gong, J. F. Wu, and E. G. Luo, "Performances of the mixed-gases Joule–Thomson refrigeration cycles for cooling fixed-temperature heat loads," *Cryogenics*, vol. 44, no. 12, pp. 847–857, Dec. 2004.

[30] G. Nellis, C. Hughes, and J. Pfotenhauer, "Heat transfer coefficient measurements for mixed gas working fluids at cryogenic temperatures," *Cryogenics*, vol. 45, no. 8, pp. 546–556, Aug. 2005.

[31] P. P. P. M. Lerou, H. J. M. ter Brake, H. J. Holland, J. F. Burger, and H. Rogalla, "Insight into clogging of micromachined cryogenic coolers," *Appl. Phys. Lett.*, vol. 90, no. 6, p. 064102, Feb. 2007.

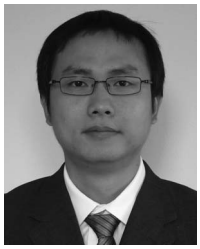

Weibin Zhu received the B.S. degree in mechatronic engineering from the South China University of Technology, Guangzhou, China, in 1999, the M.S. and Ph.D. degrees in mechanical engineering from the University of Michigan, Ann Arbor, in 2004 and 2009, respectively.

He is currently a Research Scientist with PicoCal Inc., Ann Arbor, MI. His research interest as a graduate student was micromachined Joule-Thomson cryocoolers for cryosurgical instruments. His current research projects include various MEMS applications related to thermal scanning microscopy, and bio and chemical sensing.

Michael J. White received the B.S. and M.S. degrees in mechanical engineering from the University of Wisconsin-Madison, Madison.

He is currently with the Cryogenics Department, Accelerator Division, Fermi National Accelerator Laboratory, Batavia, IL. His work is primarily focused on building the cryogenic infrastructure required for two new facilities being constructed for testing superconducting radio frequency cavities. He is also actively working on developing thermal models of accelerator components and cryogenic distribution systems for the proposed Project X. As a graduate student, his research was focused on developing a thermal model for perforated plate heat exchangers and on experimentally validating the model.

Gregory F. Nellis received the B.S. degree from the University of Wisconsin, Madison, and the M.S. and Ph.D. degrees from the Massachusetts Institute of Technology, Cambridge.

He was with the Cryogenic Engineering Lab under the advisement of Prof. J. Smith. Following graduate school, he worked for several years with Creare Inc., on the development of turbo-Brayton cryogenic refrigeration systems. He is currently an Associate Professor in mechanical engineering with the University of Wisconsin. His current projects are related to pulse-tube, mixed-gas Joule-Thomson, and active magnetic regenerative refrigeration systems. He also carries out research related to thermal-fluid issues in advanced semiconductor manufacturing techniques, such as immersion and nanoimprint lithography. He teaches classes related to thermodynamics, heat transfer, and experimental measurement systems.

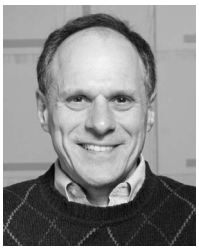

Sanford A. Klein is associated with the Solar Energy Laboratory, University of Wisconsin, Madison, and has been involved in many studies of solar and other types of energy systems. He has authored or coauthored over 150 publications relating to the analysis of energy systems. His current research interests include thermodynamics, alternative power generation systems, refrigerant properties, and alternative refrigeration systems. In addition, he is also actively involved in the development of engineering computer tools for instruction and research.

Yogesh B. Gianchandani received the B.S., M.S., and Ph.D. degrees in electrical engineering, with a focus on microelectronics and MEMS.

He is presently a Professor at the University of Michigan, Ann Arbor, with a primary appointment in the Electrical Engineering and Computer Science Department and a courtesy appointment in the Mechanical Engineering Department. He is temporarily serving at the National Science Foundation, as the program director within the Electrical, Communication, and Cyber Systems Division (ECCS).

Dr. Gianchandani's research interests include all aspects of design, fabrication, and packaging of micromachined sensors and actuators and their interface circuits (http://www.eecs.umich.edu/~yogesh/). He has published approximately 200 papers in journals and conferences, and has about 30 U.S. patents issued or pending. He was a Chief Co-Editor of *Comprehensive Microsystems: Fundamentals, Technology, and Applications*, published in 2008. He serves several journals as an editor or a member of the editorial board, and served as a General Co-Chair for the IEEE/ASME International Conference on Micro Electro Mechanical Systems (MEMS) in 2002.